AIAA JOURNAL
Vol. 37, No. 8, August 1999

Numerical Investigation of Synthetic-Jet Flowfields

Donald P. Rizzetta,* Miguel R. Visbal,† and Michael J. Stanek‡
U.S. Air Force Research Laboratory, Wright–Patterson Air Force Base, Ohio 45433-7527

The flowfields surrounding a synthetic-jet actuating device are investigated numerically by direct simulation. Solutions are obtained to the unsteady compressible Navier–Stokes equations for both the interior of the actuator cavity and for the external jet flowfield. The interior results are generated on an overset deforming zonal mesh system, whereas the jet flowfield is obtained by a high-order compact-difference scheme. Newton-like subiterations are employed to achieve second-order temporal accuracy. Details of the computations are summarized, and the quality of the results is assessed via grid resolution and time-step size studies. Several aspects of the actuator configuration are investigated, including cavity geometry and Reynolds number. Differences between two-dimensional and three-dimensional external unsteady flowfields are elucidated, and comparison is made with experimental data in terms of the mean and fluctuating components of the jet velocity.

Nomenclature

A = amplitude of cavity deformation
d = jet nozzle length
f = forcing frequency of cavity oscillation
g = analytic jet exit velocity spatial distribution
h = jet nozzle width, 0.5 mm
M_∞ = reference Mach number, 0.065
Re = reference Reynolds number, $\rho_\infty u_\infty h/\mu_\infty$
u, v, w = nondimensional Cartesian velocity components in x, y, z directions
u_∞ = reference velocity, 22.0 m/s
w' = fluctuating velocity component in the z direction
x, y, z = nondimensional Cartesian coordinates in transverse, spanwise, and streamwise directions
x_L = nondimensional cavity width
y_B = nondimensional jet nozzle half-span
z_B = nondimensional instantaneous cavity lower boundary position
z_D = nondimensional mean cavity depth
Δt = time-step size
$\Delta x, \Delta y, \Delta z$ = mesh spacing in x, y, z directions
Ω_y = component of vorticity in y direction
ω = nondimensional circular oscillation frequency, $2\pi f h/u_\infty$

Subscripts

cl = evaluated at jet centerline
j = evaluated at jet nozzle exit

Superscript

$\bar{\ }$ = time-averaged quantity

Introduction

JETS composed entirely of entrained ambient fluid may be synthesized by the formation of a time-harmonic train of vortices, which are created at the edges of a sharp orifice. Such jets operate without net mass flux across the orifice and can be produced by sound-wave transmission through the fluid, a phenomenon referred to as acoustic streaming, or by oscillation of the boundaries confining an otherwise quiescent medium. Synthetic jets may be generated for practical circumstances by a dynamic fluid actuator consisting of an enclosed cavity with a movable boundary, which is vented by a nozzle aperture. Because such devices have minimal power requirements and do not rely upon a supply of injected fluid to produce jet-like structures, they are attractive as a means of mixing enhancement in both open and closed flow systems and for convecting heat away from solid surfaces. Additional applications demonstrating active flow control include the vectoring of adjacent coflowing jets,[1] the generation of lift and drag reduction on cylinders,[2,3] the management of vortices on forebodies at high angle of attack,[4] and the delay of stall on airfoils.[5]

The development of jets with zero net mass flux have resulted from a number of investigations employing various experimental techniques. Among these are the efforts of Mednikov and Novitskii[6] who used an oscillating piston and bellows mechanism in a resonant cavity, and those of Ingard and Labate[7] applying an orifice plate to an acoustic impedance tube. Lebedeva[8] transmitted sound waves through a pipe, and Sheen et al.[9] created streaming by an oscillating ultrasonic transducer in water. More recently, James et al.[10] considered a round turbulent jet produced by a resonantly driven actuator disk.

Basic features of a synthetic-jet actuator flowfield are illustrated schematically in Fig. 1, which depicts the cross section of a three-dimensional rectangular device. The apparatus consists of a jet orifice opposed on one side by an enclosed cavity, whose lower boundary is vertically deformed in a periodic manner. Ambient fluid from above enters and exits the cavity through the jet aperture. Upward motion of the boundary produces flow, which separates at the sharp edges of the orifice and rolls into parallel vortices on either side as fluid is ejected from the cavity. These vortices then begin to propagate away from the orifice under their own self-induced velocity.[11] During downward motion of the boundary, the vortex pair has traveled sufficiently far from the orifice so as to be unaffected by the surrounding fluid that is then drawn into the cavity.

Over each cycle of operation, the net mass flux across the orifice is zero while the momentum of the vortices is nonzero. The resulting train of vortex pairs created by the actuator therefore has a time-mean streamwise velocity profile that is similar to that of a steady jet. Experimental observation[1] has indicated that, whereas the parallel vortices do not undergo pairing, they do break down and lose their individual identities at short distances from the orifice. Analysis of the frequency spectra of such jets suggests that this breakdown is caused by spanwise instabilities of the vortex cores.[1]

In addition to its utility as a control apparatus, the synthetic jet is also intriguing because of the intricate fluid physics that is exhibited in its evolution. The purpose of the work presented here is to

---

Presented as Paper 98-2910 at the AIAA 29th Fluid Dynamics Conference, Albuquerque, NM, 15–18 June 1998; received 29 June 1998; accepted for publication 27 January 1999. This paper is declared a work of the U.S. Government and is not subject to copyright protection in the United States.

*Research Aerospace Engineer, Computational Sciences Branch, Aeronautical Sciences Division. Associate Fellow AIAA.

†Technical Area Leader, Computational Sciences Branch, Aeronautical Sciences Division. Associate Fellow AIAA.

‡Aerospace Engineer, Aeromechanics Integration/Integration and Demonstration Branch, Aeronautical Sciences Division. Senior Member AIAA.

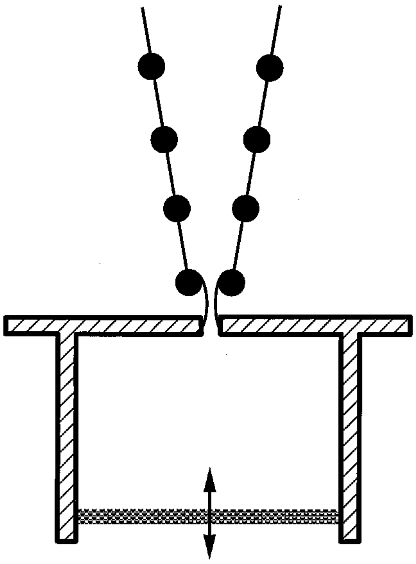

Fig. 1 Schematic diagram of synthetic-jet actuator.

investigate, by direct numerical simulation, synthetic jet flowfields that are similar to the ones studied experimentally by Smith and Glezer.[1] Those experiments considered a synthetic jet in air, which formed normal to a flat plate having a rectangular orifice with a width of 0.5 mm and a span of 75.0 mm. The Reynolds number based on the orifice width and the amplitude of the nominally time-harmonic streamwise velocity was reported to be between 500 and 1000 (Ref. 1), and the forcing frequency of the cavity is approximately 1000 Hz. Data available for comparative purposes include time-mean and fluctuating streamwise velocity distributions.

The only previous numerical simulation of a synthetic jet is by Kral et al.,[12] who computed both laminar and turbulent two-dimensional flowfields. An analytic velocity profile was assumed at the orifice exit, and the flow within the cavity was not calculated. A turbulence model was incorporated in the simulation as an artifice to increase viscous diffusion and mimic breakup of the vortex train that was observed experimentally, but not captured, by two-dimensional laminar solutions. Good agreement was obtained with measured mean velocity profiles, but no comparison with fluctuating components was provided. Imposition of similar analytic synthetic jet exit velocity profiles has also been used to computationally simulate flow control for airfoil[13] and rotorcraft[14] applications.

The current effort numerically describes the flowfield within the actuator cavity, as well as exterior to it, by obtaining solutions to the unsteady compressible Navier–Stokes equations. This is accomplished for the interior flow by use of an overset deforming zonal grid system. Solutions for the external jet flowfield are considered in both two and three spatial dimensions employing a high-order implicit compact finite-difference scheme. The computational procedure is summarized, details of the calculations are presented, and the accuracy of the numerical results is assessed via grid resolution and time-step size studies. Features of the resultant flowfields are elucidated, and comparison is made with experimental data.

Governing Equations

The most general representation of the governing equations was taken to be the unsteady three-dimensional compressible Navier–Stokes equations, written in nondimensional variables and expressed in conservative form. A general time-dependent transformation of the independent variables to surface-fitted computational coordinates was made. The resulting transformed equations included a vector source term that is required to enforce a geometric conservation law[15] for the deforming computational mesh that is used to represent the moving boundary of the actuator cavity. Complete details of the governing equations and associated boundary conditions have been omitted here for brevity, but may be found in their entirety in Ref. 16. The Sutherland law for the molecular viscosity coefficient and the perfect gas relationship were also employed, and Stokes' hypothesis for the bulk viscosity coefficient was invoked.

Numerical Procedure

Time-accurate solutions to the governing equations were obtained numerically by the implicit approximately factored finite difference algorithm of Beam and Warming,[17] which has evolved as an efficient tool for generating solutions to a wide variety of complex fluid flow problems. Second-order accurate backward-implicit time differencing was used to represent temporal derivatives. Numerical fluxes considered in the explicit portion of the algorithm were evaluated by either second-order accurate central approximations or by a high-order compact scheme.

The implicit segment of the algorithm incorporated second-order accurate centered differencing for all spatial derivatives and used nonlinear artificial dissipation[18] to augment stability. Efficiency was enhanced by solving this implicit portion of the factorized equations in diagonalized form.[19] Temporal accuracy, which was degraded because of the use of the diagonal form, was improved by performing Newton-like subiterations[20] within a time step. This technique has been commonly invoked to reduce errors caused by factorization, linearization, and explicit application of boundary conditions; it is particularly useful for achieving temporal accuracy on overset zonal mesh systems. The procedure also reduces any deterioration of the solution caused by use of artificial dissipation and by lower-order spatial resolution of implicit operators.

Simultaneous solutions for the flowfields, interior and exterior to the synthetic-jet actuator configuration, were obtained using the Chimera[21,22] overset domain decomposition methodology. Because the high-order compact difference scheme was not available for use in combination with the Chimera technique, these solutions were produced with second-order spatial accuracy. After several oscillatory cycles of the cavity boundary, however, the flowfield became essentially periodic. At this point the velocity profile across the jet nozzle exit was recorded at each time step for one complete cycle. The recorded profile was then specified as a boundary condition for the exterior domain, without the necessity for concurrently performing the deforming cavity computation. Thus the exterior flow in two and three spatial dimensions could be described with a single computational block utilizing a high-resolution spatial discretization. Because of a more efficient use of computing resources, this procedure enabled the construction of long-time two-dimensional results.

The high-order compact difference scheme is based upon the pentadiagonal system of Lele,[23] which has been adapted by Visbal and Gaitonde[24] as an implicit iterative time-marching technique applicable for unsteady vortical flows on curvilinear meshes. It is used in conjunction with a nondispersive spatial filter developed by Gaitonde et al.,[25] which has been shown to be superior to the use of artificial dissipation.

The aforementioned features of the numerical algorithm are embodied in an existing fully vectorized time-accurate three-dimensional computer code FDL3DI, which has proven to be reliable for steady and unsteady fluid flow problems, including the simulation of flows over delta wings with leading-edge vortices,[20,26,27] vortex breakdown,[27,28] and direct simulation of a transitional wall jet.[29]

Computational Meshes

Figure 2 illustrates the geometry of the actuator configuration, where a Cartesian coordinate system is oriented with its origin at the centerline of the nozzle exit, located on the midspan plane of symmetry. The jet nozzle width h was taken as 0.5 mm, consistent with the experiment of Smith and Glezer,[1] and the nozzle length was chosen to be equal to the width $(d = h)$. The nondimensional width and mean depth of the cavity are given by x_L and z_D, respectively, where $x_L = 15.0$ and two values of z_D were considered: $z_D = 10.0$, 2.0. For the three-dimensional computation the nozzle half-span length was specified as $y_B = 7.5$. Oscillation of the cavity was forced by varying the position of its lower boundary according to

$$z_B = -z_D + A\sin(\omega t) \qquad (1)$$

Table 1 Computational mesh parameters

Mesh designation	Mesh size	$\Delta x_{\min}$	$\Delta y_{\min}$	$\Delta z_{\min}$
Cavity	$(273 \times 1 \times 151)$	0.005	——	0.005
Nozzle	$(97 \times 1 \times 117)$	0.005	——	0.005
External fine	$(317 \times 1 \times 346)$	0.005	——	0.005
External coarse	$(175 \times 1 \times 173)$	0.010	——	0.010
External three-dimensional	$(88 \times 138 \times 173)$	0.010	0.075	0.010

Table 2 Configurations

Designation	*Re*	z_D
Case 1	750	10.0
Case 2	750	2.0
Case 3	1500	10.0

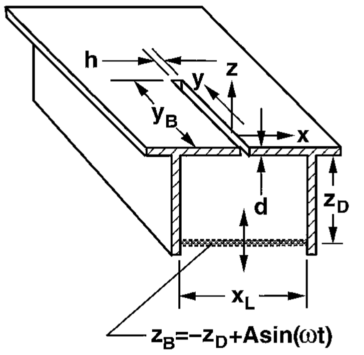

Fig. 2 Synthetic-jet actuator configuration.

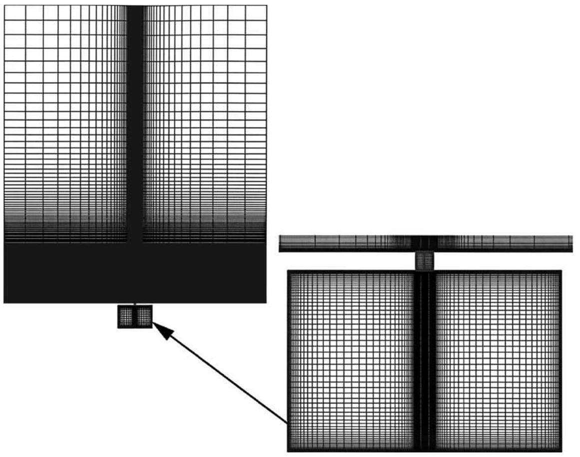

Fig. 3 Synthetic-jet computational domains.

The complete two-dimensional configuration was represented using the Chimera methodology, which allows an entire computational flowfield to be partitioned into a number of less complex overlapping or embedded regions for which grids may be more easily constructed. In the present application three distinct domains were defined, consisting of grids for the regions above the jet orifice, within the cavity, and through the connecting orifice nozzle. Table 1 provides the mesh sizes and spacings. Grids for all three domains appear in Fig. 3, where a view of the cavity region displaying only every other mesh point is seen.

Grid points in the overlapping zones were coincident in the adjacent meshes so that accuracy was not compromised because of interpolation. Transfer of information between the domains, however, was accomplished as a general feature of automated software,[30] which was used to establish donor and recipient grid points in each region. At each time step grid points of the lower cavity mesh were redistributed in the vertical direction using the stretching function of Vinokur.[31]

In the three-dimensional computation symmetry planes were imposed at the jet centerline $(x = 0)$ and at midspan $(y = 0)$, thus limiting the computational domain to one-quarter of the complete physical configuration. Apart from that consideration, the three-dimensional grid system is identical to the coarse external mesh in $x - z$ planes, which were distributed along the spanwise (y) direction.

Details of the Computations

Standard atmospheric conditions were assumed for thermodynamic variables, and the baseline Reynolds number was chosen to be 750, which is in the range of experimental measurements. This resulted in the reference values of $M_\infty = 0.065$ and $u_\infty = 22.0$ m/s, and the frequency was set to 1000 Hz. Several different configurations were investigated, which corresponded to variations in the mean cavity depth and to the nominal Reynolds number. These cases are listed in Table 2.

As noted before, the lower boundary of the cavity domain oscillated in the vertical direction as given by Eq. (1). The magnitude of the velocity at the jet exit was controlled by varying the amplitude of the forcing function A. Having fixed a reference condition, the moving boundary amplitude was adjusted until the peak-to-peak magnitude of the orifice velocity coincided with u_∞. An estimated value of A could be obtained by considering the velocity of the moving boundary and the contraction ratio of the cavity. For case 1 $A = 0.41$. This value was not changed in other situations, so that only one parameter was varied from case to case.

Flowfields for all three zones of each case were allowed to evolve for seven cycles of oscillation. Three subiterations were performed within each time step, and Δt was chosen such that each period was comprised of 4000 steps. During the eighth oscillation cycle, the jet exit velocity profile was recorded for subsequent processing.

Two-dimensional solutions were evolved for long periods of time and found to exhibit no assymetry about the jet centerline $(x = 0)$. To conserve computational resources, all of the results presented here were therefore generated by employing a symmetry condition at $x = 0$, thereby reducing the number of grid points by half. The two-dimensional flowfields obtained by specifying jet exit velocity profiles were allowed to evolve for 10 cycles of oscillation to eliminate initial transients. Another 10 cycles were calculated and used to compare the respective solutions. For the three-dimensional computation a time step corresponding to 8000 steps per cycle was employed in order to resolve the small-scale structures that appeared; however, only two subiterations were used within each time step. The compact-difference scheme was applied with fourth-order accurate spatial resolution, used in combination with an eighth-order filter for two-dimensional solutions, whereas the three-dimensional result had sixth-order accuracy with an eighth-order filter.

Quality of the Solutions

Prior to describing features of the actuator flowfields, the quality of numerical solutions is addressed via grid resolution and time-step size studies. For this purpose the computed jet orifice velocity from case 1 was imposed as a boundary condition, and only the external domain was calculated. Shown in Fig. 4 are time histories of the jet centerline velocity at two vertical locations as computed on the fine and coarse computational meshes. Only the last three oscillation cycles appear in the figure, where little variation between the histories on respective grids is observed. Because of stretching of the vertical mesh distribution, which is necessary at the upper boundary to preclude numerical anomalies, it is only possible to accurately resolve convection of the vortices for a limited distance. On the coarse mesh for at least $z < 20.0$, the resolution is adequate.

Presented in Fig. 5 are instantaneous contours of the y component of vorticity for case 1 at the end of the tenth oscillation cycle as computed on both grids. The size and shape of the vortices on each mesh are approximately the same. As a point of reference, the top of Fig. 5 is located at $z = 20$. Because the induced convective velocity of the vortices is a function of the solution, it is significant that over the same time period vortices have propagated a similar distance on each grid system.

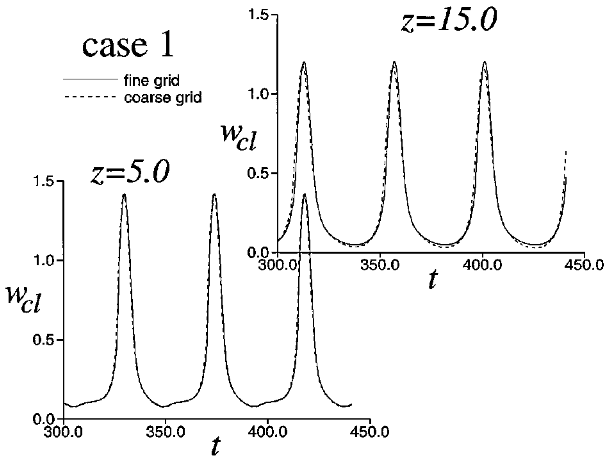

Fig. 4 Time history of centerline velocity at $z = 5.0$ and 15.0 for case 1 on the fine and coarse grids.

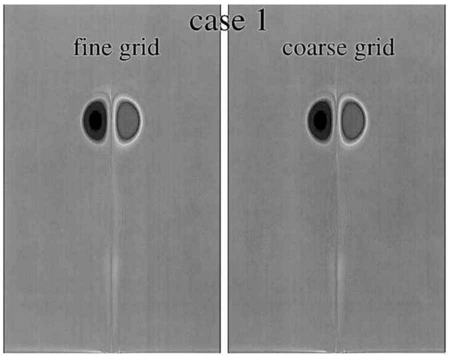

Fig. 5 Instantaneous Ω_y contours of the external flowfield on the fine and coarse grids for case 1.

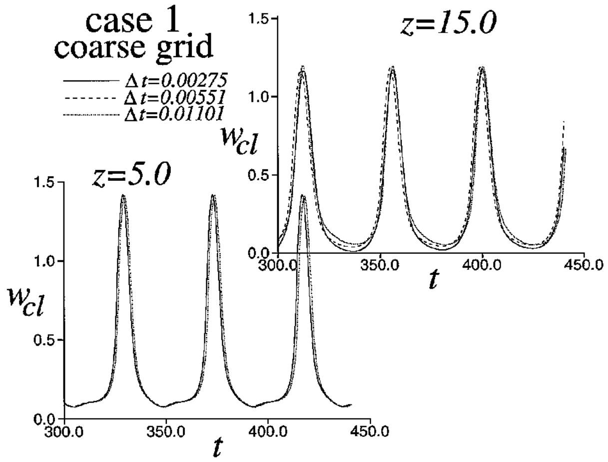

Fig. 6 Time history of the centerline velocity at $z = 5.0$ and 15.0 on the coarse grid for case 1 with $\Delta t = 0.00275$, 0.00551, and 0.01101.

Time-step size variations were performed on the coarse-grid external flowfield of case 1. Solutions were calculated using 4000, 8000, and 16000 steps per cycle by the method already described. Histories of the jet centerline velocity from these computations are found in Fig. 6 for the last three cycles. These histories were also time averaged over the ten recorded oscillation cycles and displayed as a function of time-step size in Fig. 7. This result verifies the second-order temporal accuracy of the solution by demonstrating a quadratic dependence with a vanishing slope as $\Delta t \to 0$. Instantaneous y-vorticity contours for the largest and smallest time steps are provided in Fig. 8, where the size, shape, and position of the two results are quite similar.

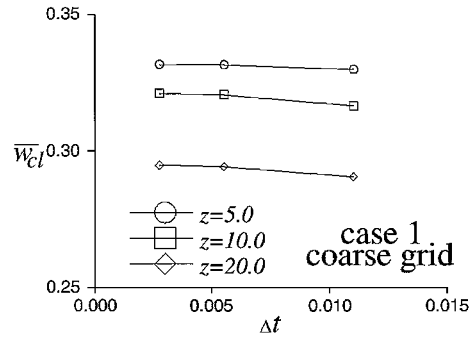

Fig. 7 Time-mean centerline velocity as a function of time step on the coarse grid for case 1.

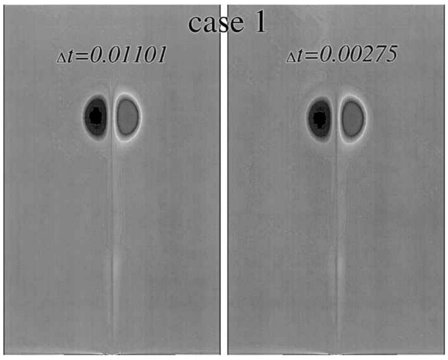

Fig. 8 Instantaneous Ω_y contours of the external flowfield on the coarse grid for case 1 with $\Delta t = 0.01101$ and 0.00275.

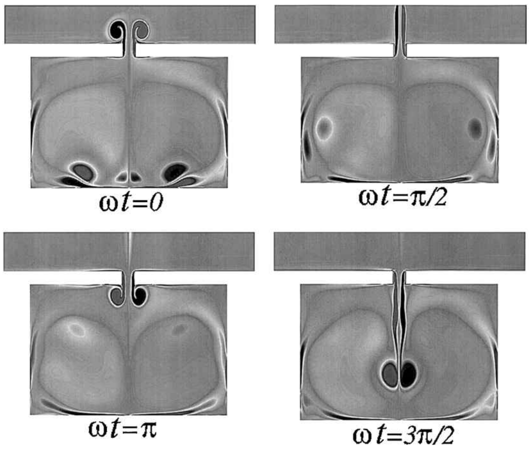

Fig. 9 Instantaneous Ω_y contours of the cavity flowfield for case 1.

Two-Dimensional Results

Instantaneous vorticity contours for the cavity flowfield are depicted in Figs. 9 and 10. For these representations the phase is referenced to the start of a cavity oscillation cycle as given by Eq. (1). Four scenes during one cycle for case 1 are indicated in Fig. 9. At any instant in time, the cavity always contains two large regions of counter-rotating fluid. When $\omega t = 0$, the jet vortices have formed at the nozzle exit. The lower boundary is now at its time-mean position and moving upward with its maximum velocity, but decelerating. The vortices have convected outside of the scene at $\omega t = \pi/2$, leaving behind a trailing shear layer. Downward motion of the boundary commences at this point, drawing fluid into the cavity. A vortex pair formed internal to the cavity during this stage with vorticities

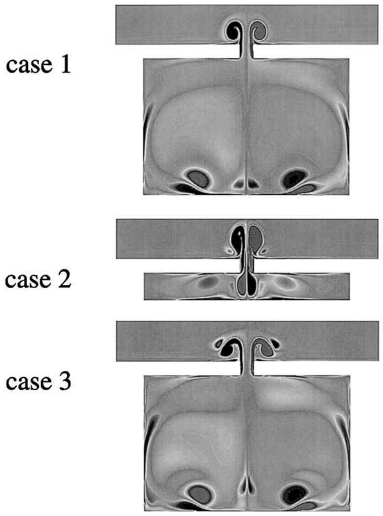

Fig. 10 Instantaneous Ω_y contours of the cavity flowfield at $\omega t = 0.0$ for cases 1, 2, and 3.

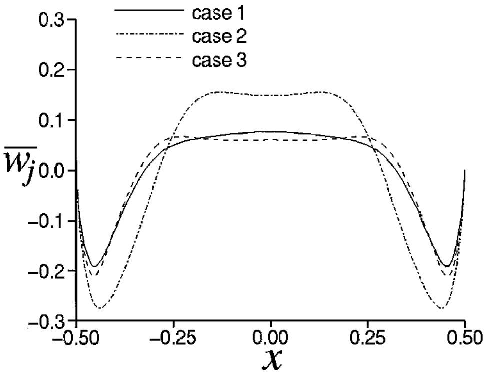

Fig. 11 Time-mean jet exit velocity profiles for cases 1, 2, and 3.

of opposite sign, respectively, to the external pair for $\omega t = 0$. They propagate into the interior as is evident when $\omega t = \pi$. The lower boundary is again at its neutral position, moving downward. The vortex pair continues its penetration into the cavity at $\omega t = 3\pi/2$ and serves to reinforce the large counter-rotating internal structures as the boundary reaches its minimum location. When the vortices collide with the lower surface, fluid next to the boundary is ejected and forms secondary separation bubbles that recirculate in directions opposite to those of the corresponding impinging vortices ($\omega t = 0$).

The view for case 1 at $\omega t = 0$ is reproduced in Fig. 10, along with similar scenes for cases 2 and 3. Because case 2 represents a much shorter cavity, but has the same forcing amplitude as case 1, a stronger vortex is generated. Also, the ingested vortex pair is compelled to remain in proximity to the cavity centerline, being constrained by the lower boundary. The higher Reynolds number of case 3 produces vortices that are less diffuse and formed by a more distinct roll up of the nozzle shear layers than was found for case 1. Lying above and outboard of the vortex pair are small regions of fluid having vorticity that is opposite in sign to that of the jet vortices. These regions are composed of the remnants of fluid that originally were ingested into the nozzle as the cavity volume increased, but subsequently were expelled. Similar regions for case 2 are also visible, where they are located somewhat below the jet vortices.

Jet exit velocity profiles are considered in Figs. 11 and 12. In addition to cases 1, 2, and 3, external flowfields were also generated by prescribing analytic descriptions for the jet exit velocity distributions. Such descriptions have been employed previously for the computation of synthetic jet flows[12–14] and can be expressed as

$$w_j = g(x)\sin(\omega t) \tag{2}$$

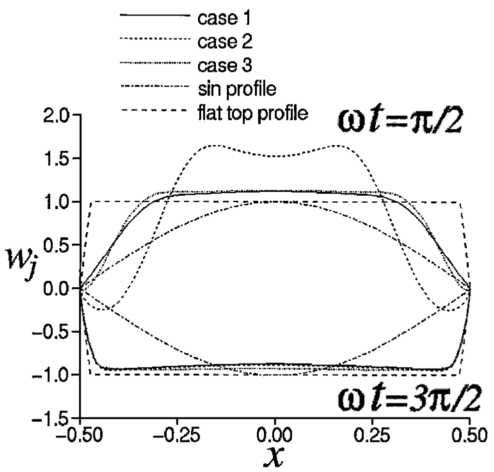

Fig. 12 Instantaneous jet exit velocity profiles for cases 1, 2 and 3 and analytic descriptions.

Two commonly used forms for $g(x)$ were specified in the present investigation: a sine profile defined by

$$g(x) = \sin\left[\pi\left(x + \tfrac{1}{2}\right)\right] \tag{3}$$

and a flat-top profile for which

$$g(x) = 1 \tag{4}$$

The flat-top profile was implemented numerically by linearly varying the uniform distribution at the edges of the jet to satisfy the no-slip condition. All of the remaining results pertain only to the external flowfields, where jet velocity profiles have been specified. For these situations the recorded jet exit velocity distributions in each case were phase translated so that $t = 0$ corresponded to a zero mass-flux condition at the nozzle exit. In this way a consistent comparison could be made between the respective cases, including the analytic descriptions of Eqs. (2–4).

Time-mean jet exit velocity distributions for cases 1, 2, and 3 are presented in Fig. 11. Although the mean net mass flux across the nozzle exit is zero, there exist regions of inflow at the edges of the orifice balanced by outflow in the center portion. This is quite different from the analytic descriptions for which $\overline{w_j} = 0$. cases 1 and 3 are quite similar, but case 2 produces larger mean inflow and outflow. Seen in Fig. 12 are instantaneous profiles of the jet velocity. Once again, cases 1 and 3 are similar. Case 2 produces a very high outflow velocity at $\omega t = \pi/2$, but an inflow velocity at $\omega t = 3\pi/2$ that is comparable to cases 1 and 3. The sine profile is observed to be unlike the computed cases whereas the flat-top profile is similar to cases 1, 2, and 3 at $\omega t = 3\pi/2$. The numerically generated distributions are not antisymmetric in time about $\omega t = \pi$ because of viscous effects. A portion of the outflowing fluid is formed by the boundary layers along the walls of the nozzle, which are absent during inflow. This effect can be expected to be more pronounced for nozzles of greater length. For case 1, however, the average peak-to-peak value of the jet amplitude is approximately 1.0, which is the condition that was enforced by adjusting A.

Figure 13 displays instantaneous vorticity contours of the case 1 exterior jet flow field for one period of the oscillation cycle. Recall that at $\omega t = 0$ the jet nozzle exit mass flux is zero, but a previously formed vortex pair is evident. New vortices are being spawned at $\omega t = \pi/2$ and have shed entirely by $\omega t = \pi$. As they move upward, a trailing viscous region can be observed, which is dissipating at $\omega t = 3\pi/2$. Displayed in Fig. 14 at $\omega t = 0$ are the flowfields for cases 1, 2, and 3, as well as that for the sine profile. Figure 14 indicates that the stronger vortices produced by the short cavity of case 2 have propagated a greater distance over the same length of time as those of case 1. In addition, the trailing shear layers generated by the convecting vortex pair contained instabilities that caused them to roll up and form a set of secondary vortices. These secondary vortices, visible in Fig. 14, are smaller and much weaker

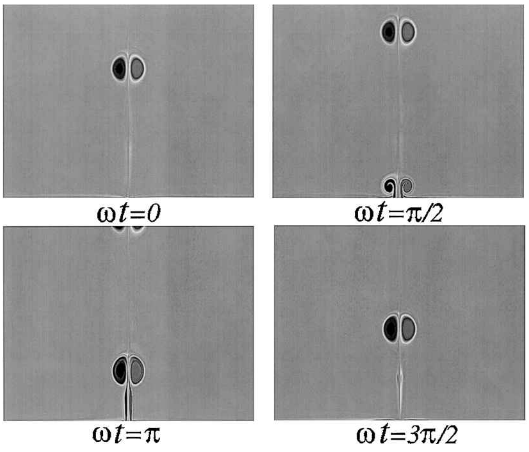

Fig. 13 Instantaneous Ω_y contours of the external flowfield for case 1.

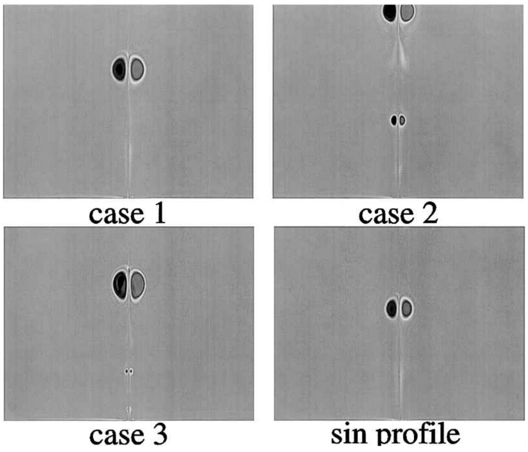

Fig. 14 Instantaneous Ω_y contours of the external flowfield at $\omega t = 0.0$ for cases 1, 2, and 3 and the sine profile.

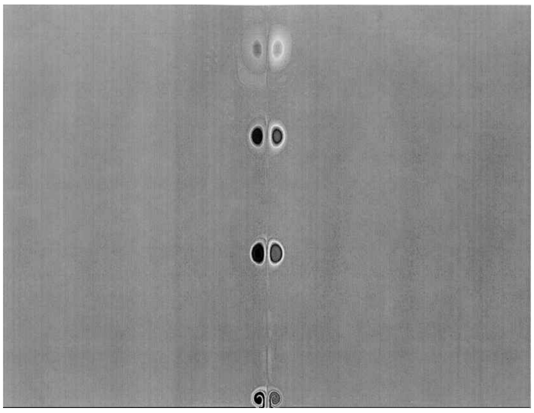

Fig. 15 Instantaneous Ω_y contours of the external flowfield at $\omega t = \pi/2$ for case 1.

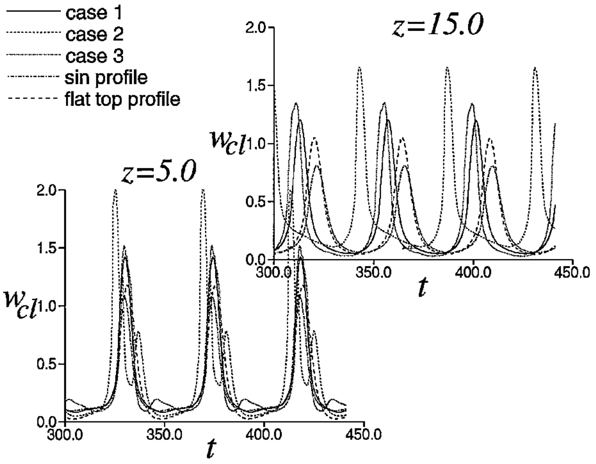

Fig. 16 Time history of the centerline velocity at $z = 5.0$ and 15.0 for cases 1, 2, and 3 and analytic descriptions.

than the primary pair, and therefore convect at a much slower rate. Eventually they are overtaken by the subsequent vortices shed at the nozzle exit and are merged into the primary set.

The corresponding case 3 flowfield shows that the vortices convect with a velocity comparable to that of case 1. Similar to case 2, a small pair of secondary vortices produced by roll up of the trailing shear layers also forms. In this situation, however, the induced velocity of the secondary vortices is so small that they remain virtually stationary at a fixed spatial location. Their convective speed is offset by that of the incoming fluid near the jet exit, and eventually they merge with a newly formed primary vortex pair. Below the small vortex pair is the remaining portion of the dissipating shear layer.

The sine profile flowfield appearing in Fig. 14 demonstrates vortices that are weaker and convecting more slowly than those of case 1. Vortices from the flat-top profile (not shown) were also found to be somewhat weaker than those of case 1.

Presented in Fig. 15 is an expanded view of the flowfield from case 1, showing the vortex train emanating from the jet exit. In this instance the top of the figure is located at $z = 45.0$. The expanded view illustrates that the high-order difference scheme is capable of resolving a series of vortices with reasonable accuracy on the stretched mesh system.

A final comparison between the flowfields resulting from the various jet exit velocity profiles is presented in Fig. 16, where the last three cycles of the centerline velocity time history is seen at two vertical locations. As noted earlier, case 2 produces the largest peak velocity magnitude. At $z = 5.0$ the case 2 history exhibits a secondary peak caused by formation of the secondary vortices. Although much smaller, a secondary peak is also evident in the case 3 history. Secondary peaks do not occur for $z = 15.0$ because at this location merging of the primary and secondary vortices has already taken place. The sine profile displays the smallest velocity magnitude. At $z = 5.0$ the case 1 maximum centerline velocity ($w_{\mathrm{cl}} \approx 1.5$) is approximately 50% higher than the jet exit velocity ($w_j \approx 1.0$) because of the combined translational velocity of the vortices plus the rotation of their cores.

Three-Dimensional Results

We have already noted that only one-quarter of the full three-dimensional synthetic-jet flowfield was simulated numerically by enforcing planes of symmetry at the jet centerline ($x = 0$) and at the midspan location ($y = 0$). Although this representation necessarily precludes asymmetric interaction between vortices on opposite sides of the centerline, no such interaction was evident in the experiment of Smith and Glezer.[1] Because of limitations of computing resources, it still was not possible to resolve the entire spanwise extent of the experimental arrangement. For this reason the jet nozzle half-span length y_B was taken to be 7.5, which is only 10% of the Smith and Glezer value. Thus, although the exact experimental configuration is not reproduced numerically, this computation serves to elucidate the evolution of three-dimensional fluid structures that do not appear in two-dimensional simulations.

Of the 138 y grid points employed in the three-dimensional computational mesh, 101 of them were uniformly distributed along the jet exit boundary. At the spanwise end of the jet exit ($y = y_B$), the instantaneous specified profile was forced to satisfy the no-slip condition. This was done by applying a hyperbolic tangent function as a factor to the profile such that at $y = 6.5$ it attained 99% of its two-dimensional value. Only one three-dimensional calculation was carried out, corresponding to the case 1 jet exit velocity profile.

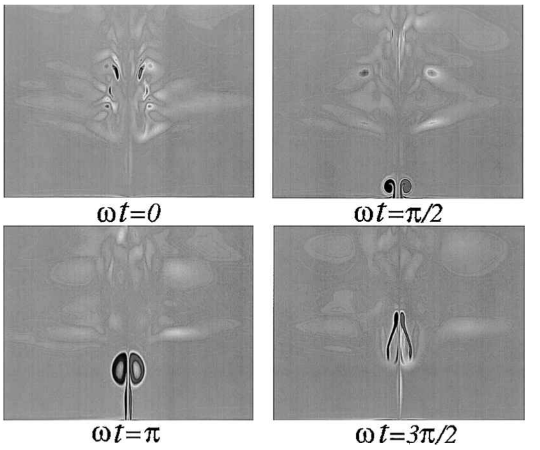

Fig. 17 Instantaneous Ω_y contours of the three-dimensional flowfield for $y = 0.0$.

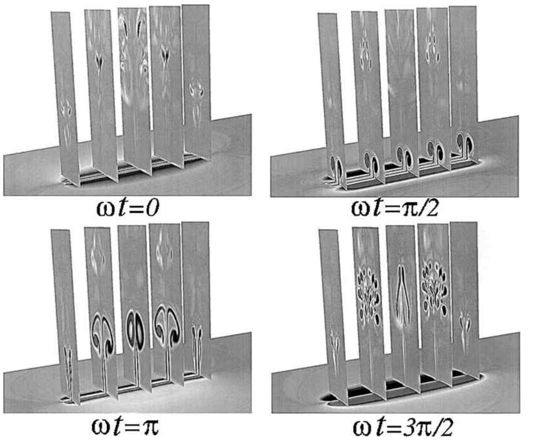

Fig. 18 Instantaneous Ω_y contours of the three-dimensional flowfield.

The computational domain was initialized with the two-dimensional solution and run for one cycle (8000 time steps) to expunge transients. Five more cycles were then computed and used to construct temporal averages.

Instantaneous contours of the y component of vorticity at the midspan location ($y = 0$) for one cycle of the three-dimensional computation are provided in Fig. 17. Once again, $t = 0$ corresponds to the zero mass-flux condition at the jet exit, so that these contours may be compared directly with the two-dimensional result in Fig. 13. At $\omega t = 0$ very little structure of the primary vortex pair is apparent. When $\omega t = \pi/2$, a new pair of vortices can be seen emerging at the nozzle exit. By $\omega t = \pi$ the vortices already appear more diffuse than their two-dimensional counterparts, with the core being encircled by a ring of higher vorticity fluid. Most of the coherent structure has vanished at $\omega t = 3\pi/2$.

In Fig. 17 only one coherent vortex pair is evident during the oscillation cycle, which is unlike the two-dimensional situation where a continuous train of vortices was observed. Experimentally, Smith and Glezer[1] also report only a single coherent vortex pair.

A three-dimensional representation of the flowfield is illustrated in Fig. 18 by instantaneous contours of the y component of vorticity at several constant spanwise locations for one cycle of the oscillation. Contours are also displayed along the lower boundary ($z = 0$), which is coincident with the plane of the nozzle exit. The one-quarter computational domain has been reflected across symmetry boundaries to create a three-dimensional depiction. Few well-defined structures are evident at $\omega t = 0$, but at $\omega t = \pi/2$ new vortices have emerged at the nozzle exit. These rapidly begin to deteriorate because of spanwise instabilities, which have the most pronounced effect at the spanwise extent of the jet exit ($y = y_B$), as is observed when $\omega t = \pi$. Here the vortex cores begin to lose strength, with their centers dissipating most rapidly. The breakup evolves toward the spanwise symmetry plane and results in the small-scale structures for $\omega t = 3\pi/2$.

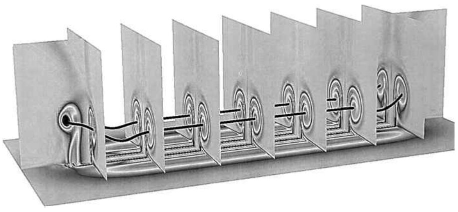

Fig. 19 Instantaneous contours of the vorticity magnitude and a vortex line for the three-dimensional flowfield at $\omega t = \pi/2$.

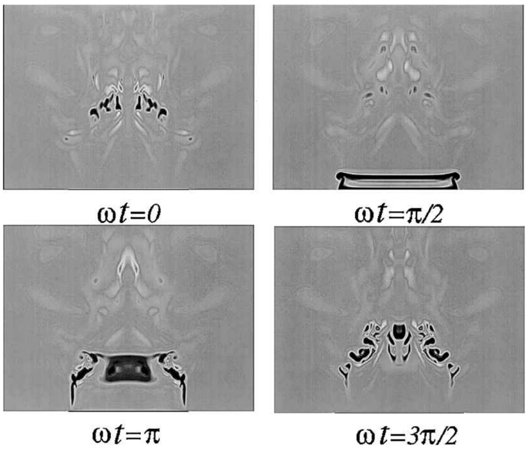

Fig. 20 Instantaneous Ω_y contours of the three-dimensional flowfield for $x = -0.5$.

An alternate portrayal of the flowfield at $\omega t = \pi/2$ is shown in Fig. 19, where instantaneous contours of the vorticity magnitude are displayed together with a vortex line that passes through the center of the vortex cores. Besides the constant spanwise planes and the lower boundary plane that were exhibited in Fig. 18, the plane of the jet centerline at $x = 0$ is also presented in Fig. 19. Because the y component of vorticity vanishes at $x = 0$, vorticity magnitude was employed as an alternative for illustrating vortical features. It is evident from the figure that as it emerges from the nozzle exit the structure should more properly be referred to as a vortex ring with a large aspect ratio or a vortex loop. The loop is seen to be quite uniform near the spanwise symmetry plane, but deforms in the far-span region. At the spanwise extent of the jet, the vortex propagates more rapidly upward than it does at the spanwise plane of symmetry.

Instantaneous vorticity contours for one oscillation cycle appear in Fig. 20 on the plane $x = -0.5$, which is located at the edge of the jet nozzle. This view again demonstrates breakup of the vortical structure because of spanwise instabilities. At $\omega t = \pi/2$ the vortex loop has emerged from the nozzle and is bent upward at the ends as was described in Fig. 19. For $\omega t = \pi$ it is apparent that the breakup moves from the ends toward the spanwise plane of symmetry. This process continues at $\omega t = 3\pi/2$, and when $\omega t = 0$ much of the original vortical form has disintegrated into finer scale structures. A spanwise bending of vortex loops is often observed experimentally.

Comparison with Experiment

Despite the fact that the present synthetic-jet computations were able to simulate the entire actuator flowfield, including the internal cavity, the configuration that was proposed does not correspond identically to the arrangement of Smith and Glezer. Details of their experimental internal mechanism are not reported in the open literature for proprietary reasons but are believed to be different than the simple enclosure assumed here. Results of two-dimensional computations indicated that exact geometric elements of the actuator cavity

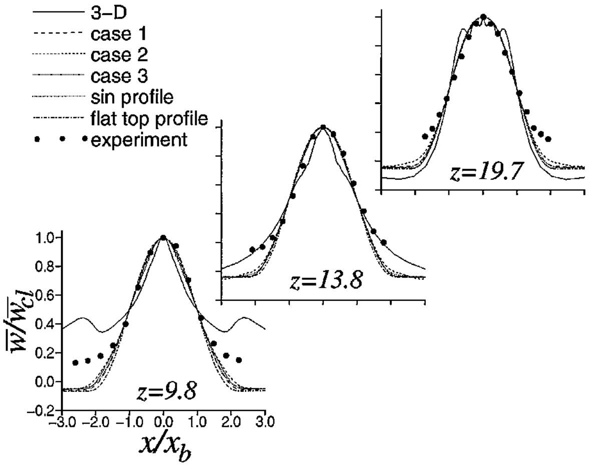

Fig. 21 Time-mean velocity profiles at $z = 9.8, 13.8, 19.7$.

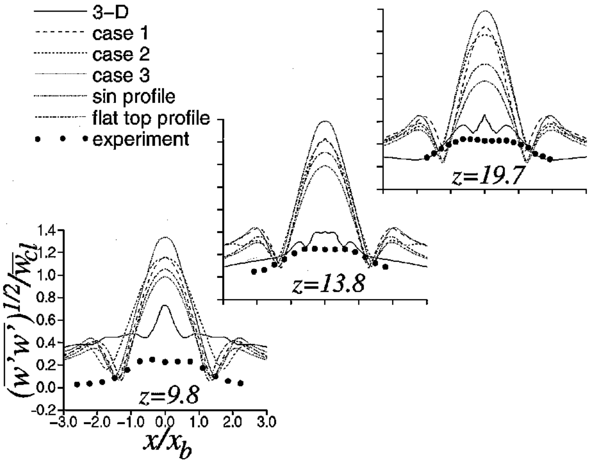

Fig. 22 Fluctuating velocity profiles at $z = 9.8, 13.8, 19.7$.

were of vital importance in determining the nozzle exit profile and subsequent synthetic-jet formation. Furthermore, the numerical jet exit aspect ratio was only one-tenth that of the experiment. Finally, although two-dimensional solutions were quite periodic in time so that meaningful temporal statistics could be obtained in several cycles of oscillation, this was not true for the three-dimensional calculation for which the frequency content was considerably higher.

Comparison of numerical results with the experimental data of Smith and Glezer[1] is provided by Fig. 21 in terms of the time-mean vertical velocity component at three streamwise locations. The comparison is formulated by use of similarity variables, which is consistent with the experimental description. Here x_b is the cross-stream jet half-width based on $\bar{w}$. All two-dimensional solutions are found in the figure, which agree well with the experiment, except at the jet lateral edges, for each streamwise position. This result agrees with the findings Kral et al.[12] Figure 21 shows that the three-dimensional result agrees only qualitatively with the data.

The root mean fluctuating component of vertical velocity at the three streamwise locations is provided in Fig. 22. All of the two-dimensional solutions produce fluctuations that are clearly larger than experimental values and are of the same magnitude as the mean component. The three-dimensional result, however, has a much smaller fluctuation owing to the spanwise instability that created a breakup of the coherent vortical structure into smaller scales; therefore, it compares more favorably with the measured data.

Conclusions

Solutions to the compressible Navier–Stokes equations were obtained for the flowfields surrounding a synthetic-jet actuating device. The interior flow was generated on an overset deforming zonal grid system while the jet flow was simulated using a high-order compact difference scheme. Both spatial and temporal quality of the results were established via mesh-size and time-step studies.

Several two-dimensional cases were investigated, corresponding to variations in the depth of the cavity and the Reynolds number, which were found to be important parameters. Resultant jet exit velocity profiles, as well as the exterior flowfields, differed from commonly employed analytic models. Jet profiles that account for the internal actuator geometry may be used as more realistic boundary conditions for practical applications.

A three-dimensional computation captured spanwise instabilities that led to a breakup of the coherent vortex structure. This phenomenon, which was postulated experimentally, cannot be reproduced in two spatial dimensions. Although it was not possible to duplicate the exact experimental configuration, the comparison with measured data was encouraging. We believe that, with sufficient computational resources and complete knowledge of physical details of the actuating device, complex synthetic-jet flowfields may be accurately simulated.

Acknowledgments

The work presented here was sponsored by the U.S. Air Force Office of Scientific Research under Task 2304 IW and was monitored by L. Sakell. Computational resources were supported in part by a grant of supercomputer time from the U.S. Department of Defense Major Shared Resource Centers at Vicksburg, Mississippi; Stennis Space Center, Mississippi; and Aberdeen Proving Ground, Maryland. The authors wish to thank B. L. Smith for providing details of the experiment and are grateful for conversations with R. B. Melville, R. E. Gordnier, and L. D. Kral.

References

[1] Smith, B. L., and Glezer, A., "Vectoring and Small-Scale Motions Effected in Free Shear Flows Using Synthetic Jet Actuators," AIAA Paper 97-0213, Jan. 1997.

[2] Amitay, M., Honohan, A., Trautman, M., and Glezer, A., "Modification of the Aerodynamic Characteristics of Bluff Bodies Using Fluidic Actuators," AIAA Paper 97-2004, June 1997.

[3] Amitay, M., Smith, B. L., and Glezer, A., "Aerodynamic Flow Control Using Synthetic Jet Technology," AIAA Paper 98-0208, Jan. 1998.

[4] Roos, F., "Synthetic-Jet Microblowing for Vortex Asymmetry Management on a Hemisphere-Cylinder Forebody," AIAA Paper 97-1973, June 1997.

[5] Smith, D. R., Amitay, M., Kibens, V., Parekh, D., and Glezer, A., "Modification of Lifting Body Aerodynamics Using Synthetic Jet Actuators," AIAA Paper 98-0209, Jan. 1998.

[6] Mednikov, E. P., and Novitskii, B. G., "Experimental Study of Intense Acoustic Streaming," *Soviet Physics—Acoustics*, Vol. 21, No. 2, 1975, pp. 152–154.

[7] Ingard, U., and Labate, S., "Acoustic Circulation Effects and the Nonlinear Impedance of Orifices," *Journal of the Acoustical Society of America*, Vol. 22, No. 2, 1950, pp. 211–218.

[8] Lebedeva, I. V., "Experimental Study of Acoustic Streaming in the Vicinity of Orifices," *Soviet Physics—Acoustics*, Vol. 26, No. 4, 1980, pp. 331–333.

[9] Sheen, S. H., Lawrence, W. P., and Raptis, A. C., "Cavitation-Controlled Ultrasonic Agitator," *Proceedings of the IEEE 1989 Ultrasonics Symposium*, Vol. 1, edited by B. R. McAvoy, Inst. of Electrical and Electronics Engineers, New York, 1989, pp. 653–656.

[10] James, R. D., Jacobs, J. W., and Glezer, A., "A Round Turbulent Jet Produced by an Oscillating Diaphragm," *Physics of Fluids A, Fluid Dynamics*, Vol. 8, No. 9, 1996, pp. 2484–2495.

[11] Glezer, A., and Coles, D., "An Experimental Study of a Turbulent Vortex Ring," *Journal of Fluid Mechanics*, Vol. 211, Feb. 1990, pp. 243–283.

[12] Kral, L. D., Donovan, J. F., Cain, A. B., and Cary, A. W., "Numerical Simulation of Synthetic Jet Actuators," AIAA Paper 97-1824, June 1997.

[13] Donovan, J. F., Kral, L. D., and Cary, A. W., "Active Flow Control Applied to an Airfoil," AIAA Paper 98-0210, Jan. 1998.

[14] Hassan, A. A., "Numerical Simulation and Potential Applications of Zero-Mass Jets for Enhanced Rotorcraft Aerodynamic Performance," AIAA Paper 98-0211, Jan. 1998.

[15] Thomas, P. D., and Lombard, C. L., "Geometric Conservation Law and Its Application to Flow Computations on Moving Grids," *AIAA Journal*, Vol. 17, No. 10, 1979, pp. 1030–1037.

[16] Rizzetta, D. P., Visbal, M. R., and Stanek, M. J., "Numerical Investigation of Synthetic Jet Flowfields," AIAA Paper 98-2910, June 1998.

[17] Beam, R., and Warming, R., "An Implicit Factored Scheme for the Compressible Navier–Stokes Equations," *AIAA Journal*, Vol. 16, No. 4, 1978, pp. 393–402.

[18] Jameson, A., Schmidt, W., and Turkel, E., "Numerical Solutions of the Euler Equations by Finite Volume Methods Using Runge–Kutta Time Stepping Schemes," AIAA Paper 81-1259, June 1981.

[19] Pulliam, T. H., and Chaussee, D. S., "A Diagonal Form of an Implicit Approximate-Factorization Algorithm," *Journal of Computational Physics*, Vol. 39, No. 2, 1981, pp. 347–363.

[20] Gordnier, R. E., and Visbal, M. R., "Numerical Simulation of Delta-Wing Roll," AIAA Paper 93-0554, Jan. 1993.

[21] Benek, J. A., Dougherty, F. C., Steger, J. L., and Buning, P. G., "Chimera: A Grid-Embedding Technique," Arnold Engineering Development Center, AEDC-TR-85-64, Arnold AFB, TN, Dec. 1985.

[22] Benek, J. A., Donegan, T. L., and Suhs, N. E., "Extended Chimera Grid Embedding Scheme with Applications to Viscous Flows," AIAA Paper 87-1126, June 1987.

[23] Lele, S. A., "Compact Finite Difference Schemes with Spectral-Like Resolution," *Journal of Computational Physics*, Vol. 103, No. 1, 1992, pp. 16–42.

[24] Visbal, M. R., and Gaitonde, D. V., "High-Order Accurate Methods for Unsteady Vortical Flows on Curvilinear Meshes," AIAA Paper 98-0131, Jan. 1998.

[25] Gaitonde, D., Shang, J. S., and Young, J. L., "Practical Aspects of High-Order Accurate Finite-Volume Schemes for Electromagnetics," AIAA Paper 97-0363, Jan. 1997.

[26] Gordnier, R. E., "Computation of Delta-Wing Roll Maneuvers," AIAA Paper 93-2975, July 1993.

[27] Visbal, M. R., "Computational Study of Vortex Breakdown on a Pitching Delta Wing," AIAA Paper 93-2974, July 1993.

[28] Visbal, M. R., "Onset of Vortex Breakdown Above a Pitching Delta Wing," *AIAA Journal*, Vol. 32, No. 8, 1994, pp. 1568–1575.

[29] Visbal, M., Gaitonde, D., and Gogineni, S., "Direct Numerical Simulation of a Forced Transitional Plane Wall Jet," AIAA Paper 98-2643, June 1998.

[30] Suhs, N. E., and Tramel, R. W., "PEGSUS 4.0 User's Manual," Arnold Engineering Development Center, AEDC-TR-91-8, Arnold AFB, TN, Oct. 1991.

[31] Vinokur, M., "One-Dimensional Stretching Functions for Finite-Difference Calculations," *Journal of Computational Physics*, Vol. 50, No. 2, 1983, pp. 215–234.

M. Sichel
Associate Editor